Title
Damping of a fluid-conveying pipe surrounded by a viscous annulus fluid

Authors
Kjolsing, Eric J
Todd, Michael D

Publication Date
2017-04-01

DOI
10.1016/j.jsv.2017.01.045

Title

Damping of a fluid-conveying pipe surrounded by a viscous annulus fluid

Author Names and Affiliations

Eric J. Kjolsing [a], Michael D. Todd [a]

[a] *Department of Structural Engineering, University of California, San Diego, La Jolla, CA 92093, USA*

Contact Information

Eric J. Kjolsing
9500 Gilman Drive, Mail Code 0085
La Jolla, CA 92093-0085
Eric.Kjolsing@gmail.com
1-858-722-4493

Michael D. Todd (Corresponding Author)
9500 Gilman Drive, Mail Code 0085
La Jolla, CA 92093-0085
mdtodd@mail.ucsd.edu
1-858-534-5951

Keywords

- Energy Harvesting
- Damping
- Fluid Conveying Pipe
- Hydrocarbon Production
- Hydrodynamic Function
- Viscous Annulus Fluid

Role of the Funding Source

Funding was provided by Los Alamos National Laboratory through the Engineering Institute under Task 5 (Subcontract No. 77137-001-11). The funding source was not involved with study design; collection, analysis or interpretation of data; in the writing of the report; or in the decision to submit the article for publication.

Abstract

To further the development of a downhole vibration based energy harvester, this study explores how fluid velocity affects damping in a fluid-conveying pipe stemming from a viscous annulus fluid. A linearized equation of motion is formed which employs a hydrodynamic forcing function to model the annulus fluid. The system is solved in the frequency domain through the use of the spectral element method. The three independent variables investigated are the conveyed fluid velocity, the rotational stiffness of the boundary (using elastic springs), and the annulus fluid viscosity. It was found that, due to the hydrodynamic functions frequency-dependence, increasing the conveyed fluid velocity increases the systems damping ratio. It was also noted that stiffer systems saw the damping ratio increase at a slower rate when compared to flexible systems as the conveyed fluid velocity was increased. The results indicate that overestimating the stiffness of a system can lead to underestimated damping ratios and that this error is made worse if the produced fluid velocity or annulus fluid viscosity is underestimated. A numeric example was provided to graphically illustrate these errors. Approved for publication, LA-UR-15-28006.

Nomenclature

Dimensional Terms

c	Viscous Damping Coefficient
c_v	Damping Coefficient
c_{cr}	Critical Damping Coefficient
d	Pipe Outer Radius
$\mathbf{d}$	Nodal Degrees of Freedom Vector
$\mathbf{d_g}$	Global Nodal Degrees of Freedom Vector
$\mathbf{f}$	Nodal Forces Vector
$\mathbf{f_g}$	Global Nodal Forces Vector
f_{hydro}	Hydrodynamic Force
g	Coefficient of Gravity
m	Mass per Unit Length of Pipe
$\bar{p}$	Mean Pressure Differential
t	Time
w	Lateral Deflection of the Pipe
x	Spatial Location Along Pipe
A, B, C	Coefficient
A_i	Flow Area
D	Confining Shell Inner Radius
E	Young's Modulus
I	Pipe Inertia
K_r	Rotational Spring Stiffness
K_t	Translational Spring Stiffness
L	Pipe Length
L^e	Spectral Element Length
M	Nodal Moment

Dimensional Terms (cont.)

M_i	Mass per Unit Length of Conveyed Fluid
Q	Nodal Shear
$\mathbf{S}$	Spectral Element Matrix
$\mathbf{S_g}$	Global Spectral Matrix
$\bar{T}$	Externally Applied Tension
U	Mean Axial Flow Velocity
$U_0 e^{\mathrm{i}\omega t}$	Pipe Velocity
$\widehat{W}$	Fourier Transform of Lateral Deflection of Pipe
ρ_e	Annulus Fluid Density
υ_e	Annulus Fluid Kinematic Viscosity
ω	Radial Frequency
ω_n	Natural Frequency

Dimensionless Terms

$\mathbf{A}$	Assembly Matrix
i	Imaginary Unit
k	Wavenumber
I_0, I_1, K_0, K_1	Modified Bessel Functions
δ	Axial Restraint Factor
ζ	Equivalent Damping Ratio
ν	Poisson Ratio
Γ	Hydrodynamic Function
Γ_i	Imaginary Part of the Hydrodynamic Function
Γ_r	Real Part of the Hydrodynamic Function

1.0 Introduction

The development of energy harvesters to power either commercially available or novel monitoring equipment has seen continued interest over the past decade [1-4]. Recently, the hydrocarbon industry has expressed interest in developing vibration based energy harvesters, capable of being deployed in the harsh downhole environment, to replace or supplement standard power sources currently in use. One possible realization is shown in Figure 1 where a well configuration has been modified to include a piezoelectric or electromagnetic harvesting system [5-11]. Bracing elements have been included above and below the energy harvester to limit fatigue damage in adjacent components due to the assumed inclusion of a mechanical amplifier [12].

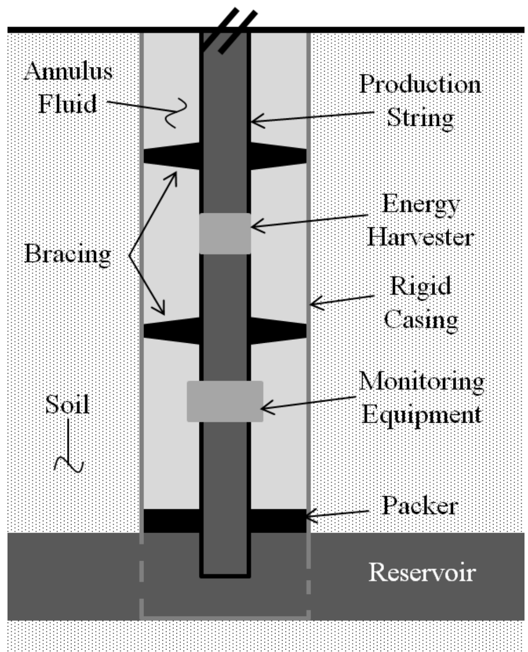

Figure 1. Modified Well Configuration.

Two important factors affect the production rate of vibration energy harvesters: the natural frequency and the damping in the structural system to which the harvester is tuned [13]. For ideal (tuned) harvesting conditions, the targeted natural frequency of the system and energy harvester would coincide (i.e. resonance), and damping in the system would be minimized (i.e. the driving accelerations would be maximized). Characterizing these two factors, then, is important in developing an optimum energy harvester for a given well configuration.

A previous investigation explored the effect axial force, annulus fluid properties, and annulus geometry had on the natural frequency of a braced well [14]. The current investigation seeks to illustrate how a pipe's conveyed fluid velocity affects damping stemming from a viscous annulus fluid. To illustrate the behavior, three variables are parametrically explored in a simple single-span model (see Figure 2): the annulus fluid viscosity, the rotational stiffness of the boundary springs, and the conveyed fluid velocity. While a multi-span model could be utilized, a single-span model is the simplest model that illustrates the behavior this investigation seeks to demonstrate.

Similar configurations have been previously investigated by others [15-23]. Kheiri et al. [24] investigated a fluid conveying pipe with flexible end restraints but did not account for a confined external fluid. Bao [25] studied submerged fluid conveying pipes on elastic supports but did not investigate damping to a significant degree.

In the current study, an Euler-Bernoulli beam formulation is employed to model the system shown in Figure 2. The spectral element method [26, 27] is used to solve the governing equation of motion. The natural frequencies and damping ratios for various systems are explored by incrementing both the stiffness of the rotational boundary springs and the conveyed fluid velocity for various annulus fluid viscosities.

A hydrodynamic forcing function is included in the model to account for viscous annulus fluid effects. The hydrodynamic function was originally introduced by Stokes [28] and later investigated by others [29-31]. Its effects have been extensively discussed and validated with experimentation [32] and finite element modeling for small amplitude vibrations [33]. It has been used by a number of researchers investigating: Fixed-Free beams [34, 35], Fixed-Pinned beams [36], and Fixed-Fixed beams [37]. Recently, the hydrodynamic function has been extensively used in investigations relating to the atomic force microscope and microcantilevers [38-42].

The following sections introduce the underlying theory and mathematical model, and then present the results of the study. The results are presented in three parts. First, the case of zero fluid flow is used to illustrate the frequency-dependent nature of the damping mechanism. Second, the effect of non-zero fluid velocity on the system damping is presented. This section also presents three-dimensional surfaces relating the conveyed fluid velocity with the two critical design parameters previously mentioned: the natural frequency and damping ratio. Lastly, a numeric example that highlights the importance of the findings is given.

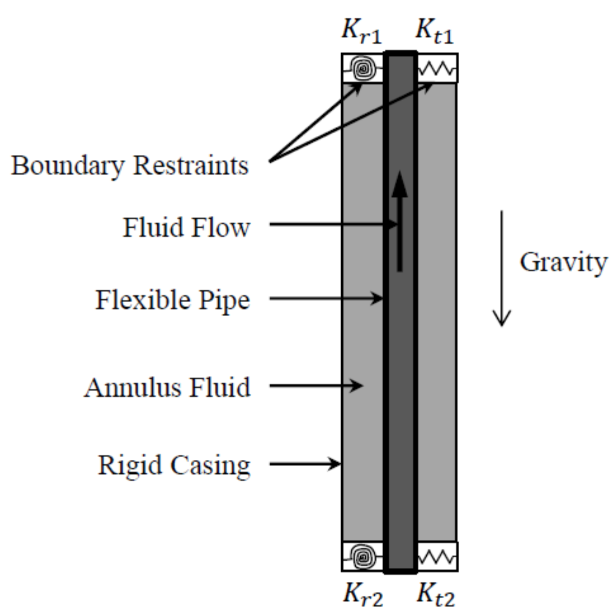

Figure 2. System Configuration.

2.0 Theory

The linearized equation of motion for a pipe conveying inviscid or viscous fluid (originally derived by Païdoussis and Issid [43]) can be modified to include annulus fluid effects. Neglecting the gravity-induced tension term (which induces a negligibly small axial load for the geometries of interest) and taking the fluid flow to be steady plug-flow, the modified equation of motion is written as

$$EIw'''' + \{M_iU^2 - \bar{T} + \bar{p}A_i(1 - 2\nu\delta)\}w'' + 2M_iU\dot{w}' + (M_i + m)gw' + c\dot{w} + (M_i + m)\ddot{w} - f_{hydro} = 0, \tag{1}$$

where prime and dot indicate derivatives with respect to spatial location and time, respectively, and positive U indicates a flow in the direction of gravity. The forces represented include a flexural restoring force, centrifugal force, externally applied tension force, tension stemming from a fluid pressure differential, Coriolis force, gravity, external viscous damping, inertia, and the hydrodynamic force generated by the annulus fluid. If desired, other flow profiles can be considered by modifying the centrifugal force with a flow-profile-modification factor [44].

The general form of the hydrodynamic force can be written as [32]

$$f_{hydro} = -\mathrm{i}\rho_e\pi d^2\omega\Gamma U_0\mathrm{e}^{\mathrm{i}\omega t}, \tag{2}$$

where $U_0\mathrm{e}^{\mathrm{i}\omega t}$ is the velocity of the oscillating pipe. The complex hydrodynamic function (Γ) and the assumptions used in the derivation of the hydrodynamic force (i.e. Eq. (2)) have been provided in Appendix A. It is well known that the real part of the hydrodynamic function (Γ_r) contributes an added mass to the system while the imaginary part (Γ_i) contributes a velocity proportional viscous drag [34].

It is important to recognize the limits of applicability of Eq. (2). The fluid equations, representing the behavior of the viscous annulus fluid, were linearized by assuming small vibration amplitudes, permitting the form of Eq. (2) presented. For large motions or behavior beyond the critical fluid velocity (i.e. divergence), the assumptions made in the derivation of the hydrodynamic forcing are violated, and Eq. (2) is no longer valid. For instance, large deflections may cause the annulus fluid to separate from the pipe's outer surface thereby changing the flow regime and violating the derivation assumptions.

Since the equation of motion is now frequency-dependent through the hydrodynamic forcing, Eq. (1) is Fourier transformed into the frequency domain

$$EI\widehat{W}'''' + \{M_iU^2 - \bar{T} + \bar{p}A_i(1 - 2\nu\delta)\}\widehat{W}'' + \{2\mathrm{i}\omega M_iU + (M_i + m)g\}\widehat{W}' + \{\mathrm{i}\omega c - (M_i + m)\omega^2 - \rho_e\pi d^2\omega^2\Gamma\}\widehat{W} = 0. \tag{3}$$

Rewriting the hydrodynamic function as $\Gamma = \Gamma_r - \mathrm{i}\Gamma_i$ and regrouping terms

$$EI\widehat{W}'''' + \{M_iU^2 - \bar{T} + \bar{p}A_i(1 - 2\nu\delta)\}\widehat{W}'' + \{2\mathrm{i}\omega M_iU + (M_i + m)g\}\widehat{W}' + \{\mathrm{i}\omega(c + \rho_e\pi d^2\omega\Gamma_i) - (M_i + m + \rho_e\pi d^2\Gamma_r)\omega^2\}\widehat{W} = 0 \tag{4}$$

the added mass and viscous drag terms become apparent. The spectral element method is employed to solve for the natural frequencies of the system [26]. The general solution to Eq. (3) is assumed to be

$$\widehat{W} = C\mathrm{e}^{\mathrm{i}kx}, \tag{5}$$

where C is a constant and k a wavenumber, leading to the dispersion relation

$$\begin{aligned} &EIk^4 - \{M_i U^2 - \bar{T} + \bar{p}A_i(1 - 2\nu\delta)\}k^2 + \{2\mathrm{i}\omega M_i U + (M_i + m)g\}\mathrm{i}k \\ &\quad + \{\mathrm{i}\omega c - (M_i + m)\omega^2 - \rho_e \pi d^2 \omega^2 \Gamma\} = 0. \end{aligned} \tag{6}$$

This fourth order equation leads to four frequency-dependent wavenumbers ($k_r, r = 1 \ldots 4$) and a new form of Eq. (5)

$$\widehat{W} = \textstyle\sum_{r=1}^{4} C_r \mathrm{e}^{\mathrm{i}k_r x} = \mathbf{eC}, \tag{7}$$

where

$$\begin{aligned} \mathbf{e} &= \left\{\mathrm{e}^{\mathrm{i}k_1 x}\ \mathrm{e}^{\mathrm{i}k_2 x}\ \mathrm{e}^{\mathrm{i}k_3 x}\ \mathrm{e}^{\mathrm{i}k_4 x}\right\}, \\ \mathbf{C} &= \{C_1, C_2, C_3, C_4\}. \end{aligned} \tag{8}$$

For a single spectral element, the nodal degrees of freedom and force vectors can be written as

$$\begin{aligned} \mathbf{d} &= \left\{\widehat{W}(0), \widehat{W}'(0), \widehat{W}(L^e), \widehat{W}'(L^e)\right\}, \\ \mathbf{f} &= \{Q(0), -M(0), -Q(L^e), M(L^e)\}, \end{aligned} \tag{9}$$

with the force relations given as [45]

$$\begin{aligned} Q &= EI\widehat{W}''' - \bar{T}\widehat{W}', \\ M &= EI\widehat{W}''. \end{aligned} \tag{10}$$

Eq. (9) can be rewritten as

$$\begin{aligned} \mathbf{d} &= \left\{\widehat{W}(0), \widehat{W}'(0), \widehat{W}(L^e), \widehat{W}'(L^e)\right\} = \{\mathbf{e}(0), \mathbf{e}'(0), \mathbf{e}(L^e), \mathbf{e}'(L^e)\}\mathbf{C} = \mathbf{HC}, \\ \mathbf{f} &= \{Q(0), -M(0), -Q(L^e), M(L^e)\} = \mathbf{XC}, \end{aligned} \tag{11}$$

where

$$\mathbf{H} = \begin{bmatrix} 1 & 1 & 1 & 1 \\ \mathrm{i}k_1 & \mathrm{i}k_2 & \mathrm{i}k_3 & \mathrm{i}k_4 \\ \mathrm{e}^{\mathrm{i}k_1 L^e} & \mathrm{e}^{\mathrm{i}k_2 L^e} & \mathrm{e}^{\mathrm{i}k_3 L^e} & \mathrm{e}^{\mathrm{i}k_4 L^e} \\ \mathrm{i}k_1\mathrm{e}^{\mathrm{i}k_1 L^e} & \mathrm{i}k_2\mathrm{e}^{\mathrm{i}k_2 L^e} & \mathrm{i}k_3\mathrm{e}^{\mathrm{i}k_3 L^e} & \mathrm{i}k_4\mathrm{e}^{\mathrm{i}k_4 L^e} \end{bmatrix}, \tag{12}$$

$$\mathbf{X} = \begin{bmatrix} g_1 & g_2 & g_3 & g_4 \\ -h_1 & -h_2 & -h_3 & -h_4 \\ -g_1 \mathrm{e}^{\mathrm{i}k_1 L^e} & -g_2 \mathrm{e}^{\mathrm{i}k_2 L^e} & -g_3 \mathrm{e}^{\mathrm{i}k_3 L^e} & -g_4 \mathrm{e}^{\mathrm{i}k_4 L^e} \\ h_1 \mathrm{e}^{\mathrm{i}k_1 L^e} & h_2 \mathrm{e}^{\mathrm{i}k_2 L^e} & h_3 \mathrm{e}^{\mathrm{i}k_3 L^e} & h_4 \mathrm{e}^{\mathrm{i}k_4 L^e} \end{bmatrix},$$

$$g_r = -\mathrm{i}k_r^3 EI - \mathrm{i}k_r \bar{T},$$

$$h_r = -k_r^2 EI.$$

Eq. (11) can be rewritten through the constants vector $\mathbf{C}$ as

$$\mathbf{f} = \mathbf{XC} = \mathbf{X}(\mathbf{H}^{-1}\mathbf{d}) = \mathbf{Sd}, \tag{13}$$

where $\mathbf{S} = \mathbf{XH}^{-1}$ is the spectral element matrix.

The individual spectral element matrices are assembled into a global dynamic stiffness matrix ($\mathbf{S_g}$) in a manner analogous to the finite element method. For a three-element model, as shown in Figure 3, the following assembly can be utilized

$$\mathbf{S_g} = \mathbf{A_1^T S^1 A_1} + \mathbf{A_2^T S^2 A_2} + \mathbf{A_3^T S^3 A_3}, \tag{14}$$

where

$$\mathbf{A_1} = \begin{bmatrix} 1 & 0 & 0 & 0 & 0 & 0 & 0 & 0 \\ 0 & 1 & 0 & 0 & 0 & 0 & 0 & 0 \\ 0 & 0 & 1 & 0 & 0 & 0 & 0 & 0 \\ 0 & 0 & 0 & 1 & 0 & 0 & 0 & 0 \end{bmatrix},$$

$$\mathbf{A_2} = \begin{bmatrix} 0 & 0 & 1 & 0 & 0 & 0 & 0 & 0 \\ 0 & 0 & 0 & 1 & 0 & 0 & 0 & 0 \\ 0 & 0 & 0 & 0 & 1 & 0 & 0 & 0 \\ 0 & 0 & 0 & 0 & 0 & 1 & 0 & 0 \end{bmatrix}, \tag{15}$$

$$\mathbf{A_3} = \begin{bmatrix} 0 & 0 & 0 & 0 & 1 & 0 & 0 & 0 \\ 0 & 0 & 0 & 0 & 0 & 1 & 0 & 0 \\ 0 & 0 & 0 & 0 & 0 & 0 & 1 & 0 \\ 0 & 0 & 0 & 0 & 0 & 0 & 0 & 1 \end{bmatrix},$$

and $\mathbf{S^1}$, $\mathbf{S^2}$, and $\mathbf{S^3}$ are the spectral element matrices for elements one, two, and three, respectively. This assembly leads to the global dynamic stiffness matrix

$$\mathbf{S_g} = \begin{bmatrix} S_{11}^1 & S_{12}^1 & S_{13}^1 & S_{14}^1 & 0 & 0 & 0 & 0 \\ S_{21}^1 & S_{22}^1 & S_{23}^1 & S_{24}^1 & 0 & 0 & 0 & 0 \\ S_{31}^1 & S_{32}^1 & S_{33}^1 + S_{11}^2 & S_{34}^1 + S_{12}^2 & S_{13}^2 & S_{14}^2 & 0 & 0 \\ S_{41}^1 & S_{42}^1 & S_{43}^1 + S_{21}^2 & S_{44}^1 + S_{22}^2 & S_{23}^2 & S_{24}^2 & 0 & 0 \\ 0 & 0 & S_{31}^2 & S_{32}^2 & S_{33}^2 + S_{11}^3 & S_{34}^2 + S_{12}^3 & S_{13}^3 & S_{14}^3 \\ 0 & 0 & S_{41}^2 & S_{42}^2 & S_{43}^2 + S_{21}^3 & S_{44}^2 + S_{22}^3 & S_{23}^3 & S_{24}^3 \\ 0 & 0 & 0 & 0 & S_{31}^3 & S_{32}^3 & S_{33}^3 & S_{34}^3 \\ 0 & 0 & 0 & 0 & S_{41}^3 & S_{42}^3 & S_{43}^3 & S_{44}^3 \end{bmatrix}. \tag{16}$$

The relevant spectral equation is given as

$$\mathbf{f_g} = \mathbf{S_g d_g}. \tag{17}$$

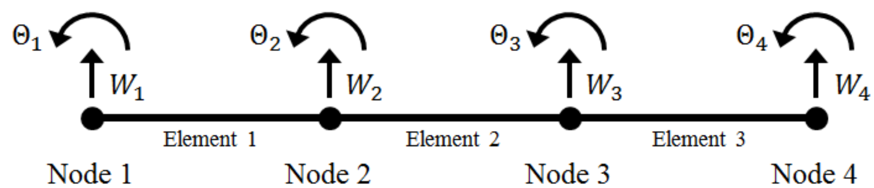

Figure 3. Three-Element Beam Model.

2.1 Structural Boundary Conditions

Structural boundary conditions can be incorporated directly into the global dynamic stiffness matrix. Consider the system shown in Figure 4 where nodal springs have been added to node one and node four. The springs, with stiffness K_{t1}, K_{r1}, K_{t2}, and K_{r2}, are attached at new nodal points with degrees of freedom W_5, Θ_5, W_6, and Θ_6.

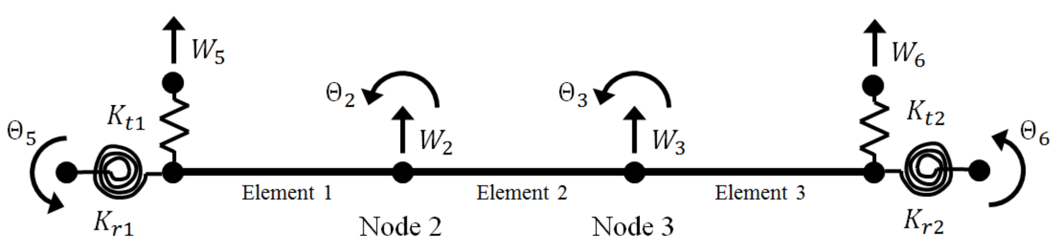

Figure 4. Three-Element Beam Model with Nodal Springs.

Analyzing the translational springs shown in Figure 5, the resulting spring equations are

$$\begin{bmatrix} Q_1 \\ Q_5 \end{bmatrix} = \begin{bmatrix} K_{t1} & -K_{t1} \\ -K_{t1} & K_{t1} \end{bmatrix} \begin{bmatrix} W_1 \\ W_5 \end{bmatrix},$$
$$\begin{bmatrix} Q_4 \\ Q_6 \end{bmatrix} = \begin{bmatrix} K_{t2} & -K_{t2} \\ -K_{t2} & K_{t2} \end{bmatrix} \begin{bmatrix} W_4 \\ W_6 \end{bmatrix}. \tag{18}$$

Similarly, the rotational spring equations can be found as

$$
\begin{aligned}
\begin{bmatrix} M_1 \\ M_5 \end{bmatrix} &= \begin{bmatrix} K_{r1} & -K_{r1} \\ -K_{r1} & K_{r1} \end{bmatrix} \begin{bmatrix} \Theta_1 \\ \Theta_5 \end{bmatrix}, \\
\begin{bmatrix} M_4 \\ M_6 \end{bmatrix} &= \begin{bmatrix} K_{r2} & -K_{r2} \\ -K_{r2} & K_{r2} \end{bmatrix} \begin{bmatrix} \Theta_4 \\ \Theta_6 \end{bmatrix}.
\end{aligned}
\tag{19}
$$

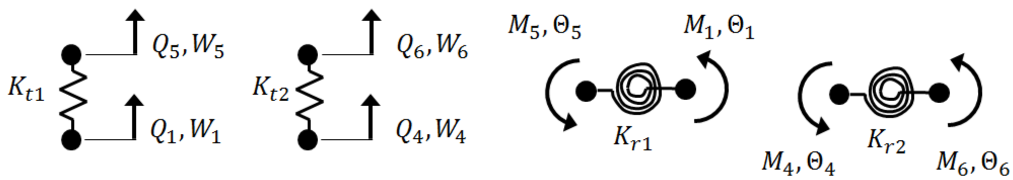

Figure 5. Free Body of Boundary Springs.

Expanding the general spectral equation (Eq. (17)) for the new configuration leads to

$$
\mathbf{f_g} = \begin{bmatrix} Q_1 \\ M_1 \\ Q_2 \\ M_2 \\ Q_3 \\ M_3 \\ Q_4 \\ M_4 \\ Q_5 \\ M_5 \\ Q_6 \\ M_6 \end{bmatrix}, \quad \mathbf{d_g} = \begin{bmatrix} W_1 \\ \Theta_1 \\ W_2 \\ \Theta_2 \\ W_3 \\ \Theta_3 \\ W_4 \\ \Theta_4 \\ W_5 \\ \Theta_5 \\ W_6 \\ \Theta_6 \end{bmatrix},
$$

$$
\mathbf{S_g} = \begin{bmatrix}
S_{11}^1 + K_{t1} & S_{12}^1 & S_{13}^1 & S_{14}^1 & 0 & 0 & 0 & 0 & -K_{t1} & 0 & 0 & 0 \\
S_{21}^1 & S_{22}^1 + K_{r1} & S_{23}^1 & S_{24}^1 & 0 & 0 & 0 & 0 & 0 & -K_{r1} & 0 & 0 \\
S_{31}^1 & S_{32}^1 & S_{33}^1 + S_{11}^2 & S_{34}^1 + S_{12}^2 & S_{13}^2 & S_{14}^2 & 0 & 0 & 0 & 0 & 0 & 0 \\
S_{41}^1 & S_{42}^1 & S_{43}^1 + S_{21}^2 & S_{44}^1 + S_{22}^2 & S_{23}^2 & S_{24}^2 & 0 & 0 & 0 & 0 & 0 & 0 \\
0 & 0 & S_{31}^2 & S_{32}^2 & S_{33}^2 + S_{11}^3 & S_{34}^2 + S_{12}^3 & S_{13}^3 & S_{14}^3 & 0 & 0 & 0 & 0 \\
0 & 0 & S_{41}^2 & S_{42}^2 & S_{43}^2 + S_{21}^3 & S_{44}^2 + S_{22}^3 & S_{23}^3 & S_{24}^3 & 0 & 0 & 0 & 0 \\
0 & 0 & 0 & 0 & S_{31}^3 & S_{32}^3 & S_{33}^3 + K_{t2} & S_{34}^3 & 0 & 0 & -K_{t2} & 0 \\
0 & 0 & 0 & 0 & S_{41}^3 & S_{42}^3 & S_{43}^3 & S_{44}^3 + K_{r2} & 0 & 0 & 0 & -K_{r2} \\
-K_{t1} & 0 & 0 & 0 & 0 & 0 & 0 & 0 & K_{t1} & 0 & 0 & 0 \\
0 & -K_{r1} & 0 & 0 & 0 & 0 & 0 & 0 & 0 & K_{r1} & 0 & 0 \\
0 & 0 & 0 & 0 & 0 & 0 & -K_{t2} & 0 & 0 & 0 & K_{t2} & 0 \\
0 & 0 & 0 & 0 & 0 & 0 & 0 & -K_{r2} & 0 & 0 & 0 & K_{r2}
\end{bmatrix}.
\tag{20}
$$

If nodes five and six are fixed, matrix reduction can be used to reduce Eq. (20). This leads to the final form of Eq. (17)

$$
\begin{bmatrix} Q_1 \\ M_1 \\ Q_2 \\ M_2 \\ Q_3 \\ M_3 \\ Q_4 \\ M_4 \end{bmatrix} = \begin{bmatrix}
S_{11}^1 + K_{t1} & S_{12}^1 & S_{13}^1 & S_{14}^1 & 0 & 0 & 0 & 0 \\
S_{21}^1 & S_{22}^1 + K_{r1} & S_{23}^1 & S_{24}^1 & 0 & 0 & 0 & 0 \\
S_{31}^1 & S_{32}^1 & S_{33}^1 + S_{11}^2 & S_{34}^1 + S_{12}^2 & S_{13}^2 & S_{14}^2 & 0 & 0 \\
S_{41}^1 & S_{42}^1 & S_{43}^1 + S_{21}^2 & S_{44}^1 + S_{22}^2 & S_{23}^2 & S_{24}^2 & 0 & 0 \\
0 & 0 & S_{31}^2 & S_{32}^2 & S_{33}^2 + S_{11}^3 & S_{34}^2 + S_{12}^3 & S_{13}^3 & S_{14}^3 \\
0 & 0 & S_{41}^2 & S_{42}^2 & S_{43}^2 + S_{21}^3 & S_{44}^2 + S_{22}^3 & S_{23}^3 & S_{24}^3 \\
0 & 0 & 0 & 0 & S_{31}^3 & S_{32}^3 & S_{33}^3 + K_{t2} & S_{34}^3 \\
0 & 0 & 0 & 0 & S_{41}^3 & S_{42}^3 & S_{43}^3 & S_{44}^3 + K_{r2}
\end{bmatrix} \begin{bmatrix} W_1 \\ \Theta_1 \\ W_2 \\ \Theta_2 \\ W_3 \\ \Theta_3 \\ W_4 \\ \Theta_4 \end{bmatrix},
\tag{21}
$$

where the contribution from nodal springs at nodes one and four are apparent.

2.2 Fluid Boundary Conditions

The importance of the fluid boundary conditions have been illustrated by Kuiper et al. [46] and Païdoussis et al. [47], where it was shown that fluid boundary conditions may have a significant impact on the systems behavior. For the current study, the conveyed fluid at the inlet and outlet is assumed to be in a flow direction tangential to the deformed pipe, which is restrained from transverse displacements at the boundaries (i.e., the momentum of the fluid is assumed not to change at the boundaries – the fluid is imagined to be flowing into adjacent lengths of equally-pressurized pipe with slope continuity at the boundaries). While a larger multi-span model may provide a more realistic representation of the in-situ system (see Figure 1), the added complexity distracts from the emphasis of the current findings, which are sufficiently conveyed with the simple model shown in Figure 2.

2.3 Calculating the Damping Ratio

By setting the determinant of the global dynamic stiffness matrix to zero

$$det\mathbf{S_g}(\omega) = 0, \tag{22}$$

the natural frequencies of the system can be determined for each mode of interest; the frequencies are real for undamped systems and contain both real and imaginary parts for systems with damping. For undamped systems, the Mathematica root solver "FindRoot" can be employed. For damped systems, the argument is taken to be complex (i.e. $\omega_d + \mathrm{i}\omega_i$) and a brute force method is used where ω_d (the damped frequency) and ω_i (corresponding to the rate of decay in the amplitude of vibration) are iterated until Eq. (22) is approximately satisfied. For the current study, Mathematica (version 9.0) is used to perform the iterative calculation.

For underdamped systems, the relationship between ω_d, ω_i, ω_n, and ζ is generally known to be

$$\begin{aligned} \omega_d &= \sqrt{1-\zeta^2}\omega_n, \\ \omega_i &= \zeta\omega_n. \end{aligned} \tag{23}$$

Squaring and then adding both equations in Eq. (**23**) leads to

$$\omega_n = \sqrt{\omega_d^2 + \omega_i^2}, \tag{24}$$

which allows the damping ratio to be written as

$$\zeta = \sqrt{1-\left(\frac{\omega_d}{\omega_n}\right)^2} = \frac{\omega_i}{\omega_n}. \tag{25}$$

Alternatively, when the damping ratio is small (i.e. $\omega_i \ll \omega_d \sim \omega_n$), the Coriolis force does no work [48, 49], and a viscous damping term (c) is not included in the system, satisfactory results can be found using the hydrodynamic function directly [32].

3.0 Results & Discussion

In total, four different annulus fluid viscosities are investigated over a range of boundary conditions and conveyed fluid velocities. Only the first mode is investigated in each case as research indicates that three-dimensional effects become non-trivial for higher order modes when employing a hydrodynamic function [38, 41]. The inputs for the various models can be found in Appendix B.

3.1 The Damping Ratio: Zero Fluid Flow

Three different annulus fluid viscosities are investigated for the case of zero conveyed fluid velocity: high, moderate, and low viscosity fluids (HVF, MVF, LVF respectively). For each system, the two rotational boundary springs are incrementally increased and both the natural frequency and damping ratio calculated as previously described. The resulting three-dimensional surfaces relate the rotational boundary stiffness to the systems natural frequency and damping ratio; the three-dimensional surfaces for the moderate viscosity fluid are shown in Figure 6 and Figure 7. Note that the four limiting boundary conditions (Pinned-Pinned, Fixed-Pinned, Pinned-Fixed, and Fixed-Fixed) are identified.

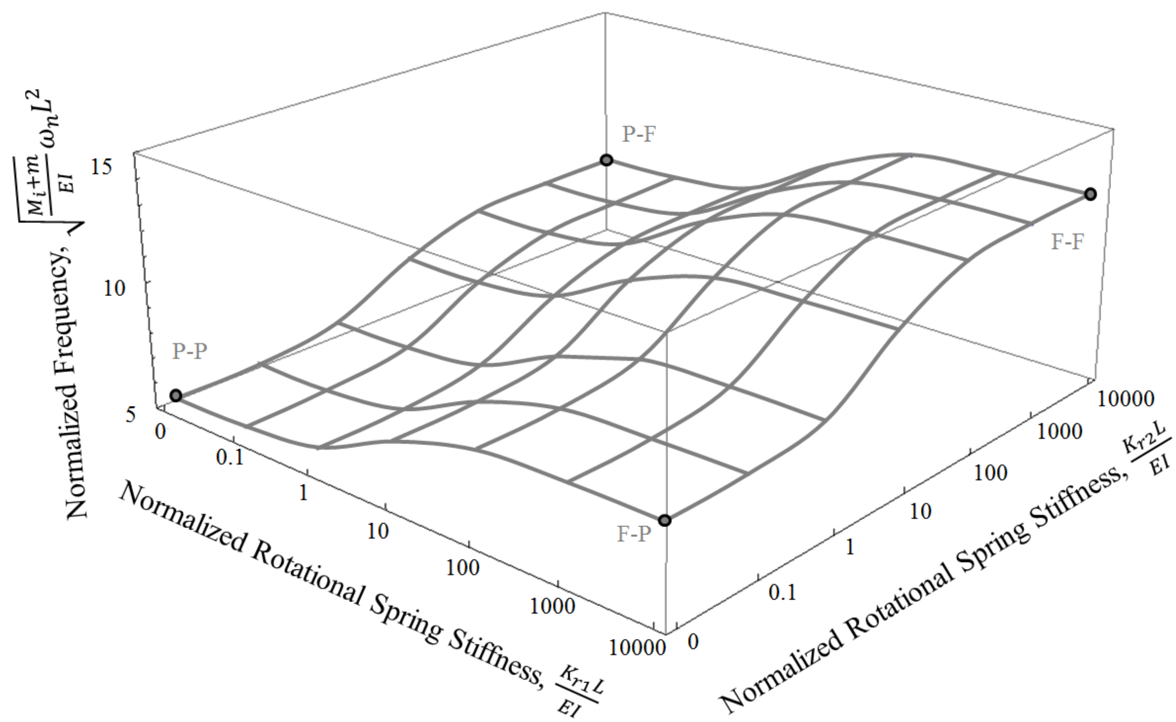

Figure 6. Rotational Spring Stiffness (K_r) vs. Natural Frequency (ω_n) for Zero Fluid Velocity - Moderate Viscosity Fluid.

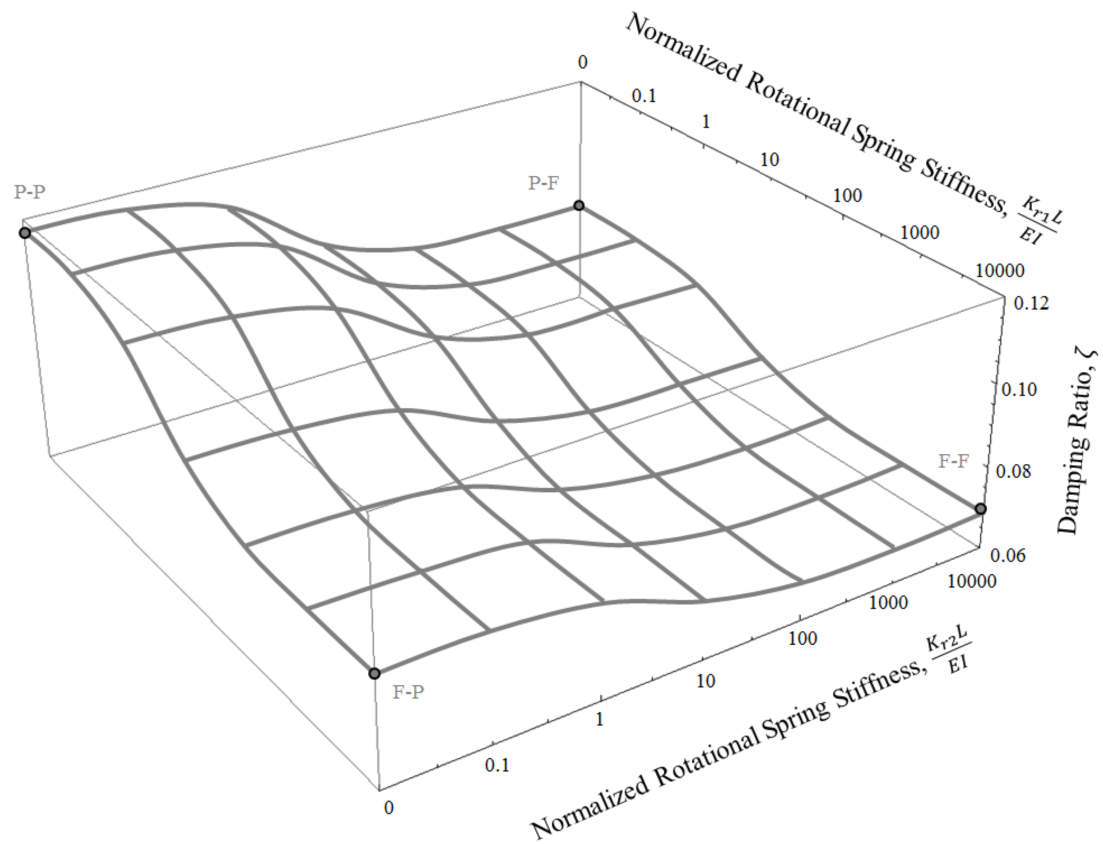

Figure 7. Rotational Spring Stiffness (K_r) vs. Damping Ratio (ζ) for Zero Fluid Velocity - Moderate Viscosity Fluid.

To better illustrate the behavior of the three systems (HVF, MVF, and LVF), two-dimensional plots are generated by taking three sections through each three-dimensional surface. The results for all three annulus fluid viscosities are presented in Figure 8 and Figure 9 where for the same fluid viscosity Figure 9 indicates stiffer systems result in lower damping ratios: $\zeta_{FF} < \zeta_{FP} = \zeta_{PF} < \zeta_{PP}$.

The damping ratios dependence on frequency is shown in Figure 10, where Eq. (25) and the relevant inputs from Appendix B have been used. It is apparent that the damping ratio is frequency-dependent through the hydrodynamic function with systems operating at a higher frequency (e.g. those with stiff rotational boundary springs) experiencing less damping. Noting the relatively constant nature of Γ_r over the range of interest shown (see Figure 11), the change in damping is primarily attributed to the change in Γ_i where, as previously mentioned, Γ_i is known to contribute viscous drag to the system.

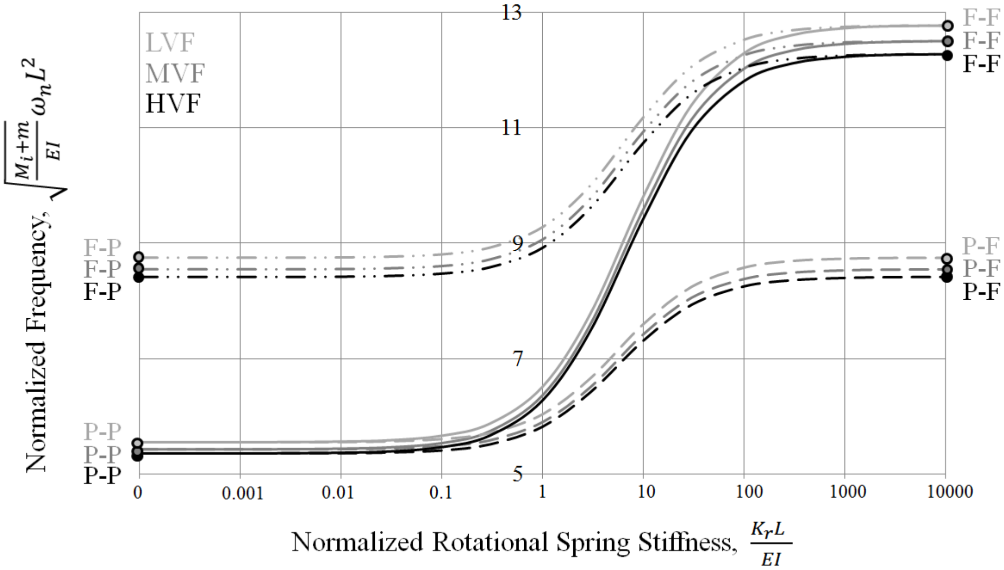

Figure 8. Rotational Spring Stiffness (K_r) vs. Natural Frequency (ω_n) for Zero Fluid Velocity. ———— **,** $K_{r1} = K_{r2} = K_r$; — — — **,** $K_{r1} = 0$ **(Pinned) &** $K_{r2} = K_r$; ·—··— **,** $K_{r1} = 10000$ **(Fixed) &** $K_{r2} = K_r$.

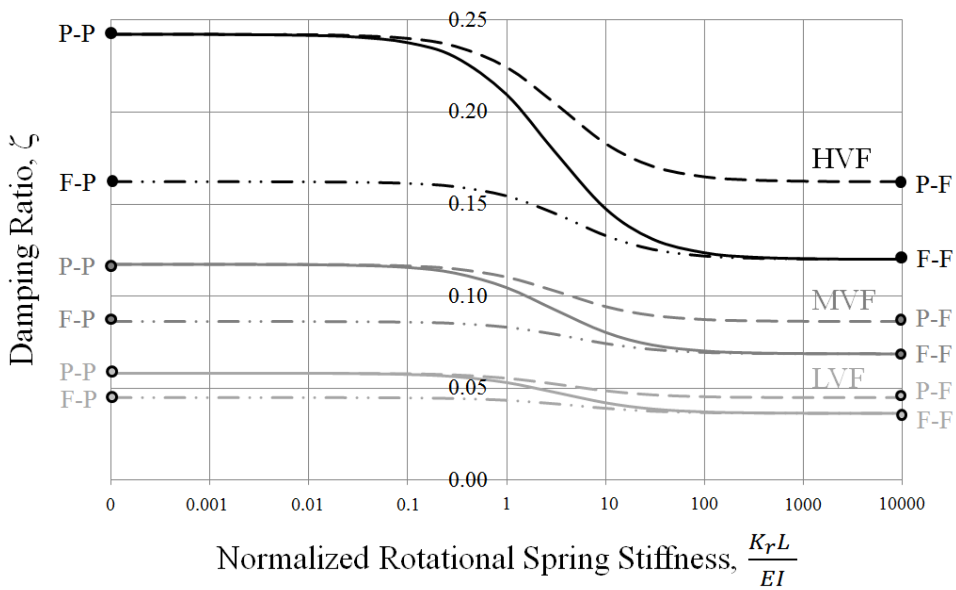

Figure 9. Rotational Spring Stiffness (K_r) vs. Damping Ratio (ζ) for Zero Fluid Velocity. ———— **,** $K_{r1} = K_{r2} = K_r$; — — — **,** $K_{r1} = 0$ **(Pinned) &** $K_{r2} = K_r$; ·—··— **,** $K_{r1} = 10000$ **(Fixed) &** $K_{r2} = K_r$.

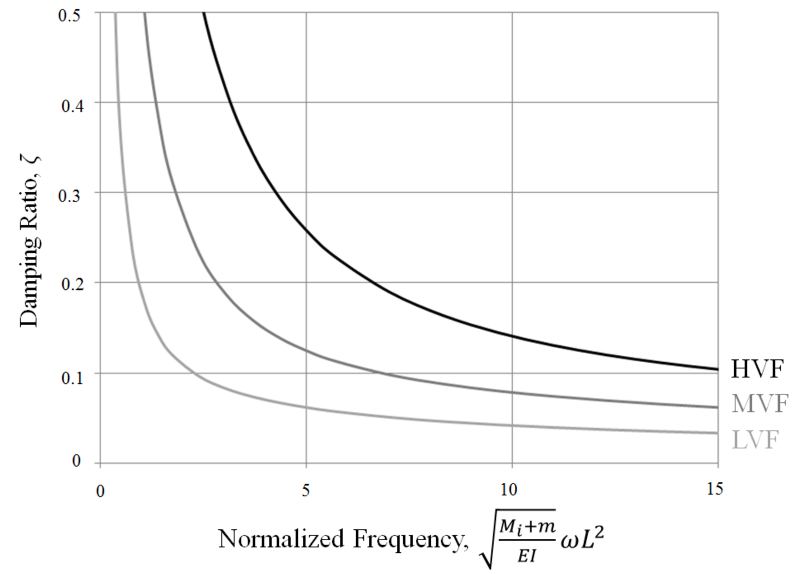

Figure 10. Damping Ratio for Arbitrary Frequencies.

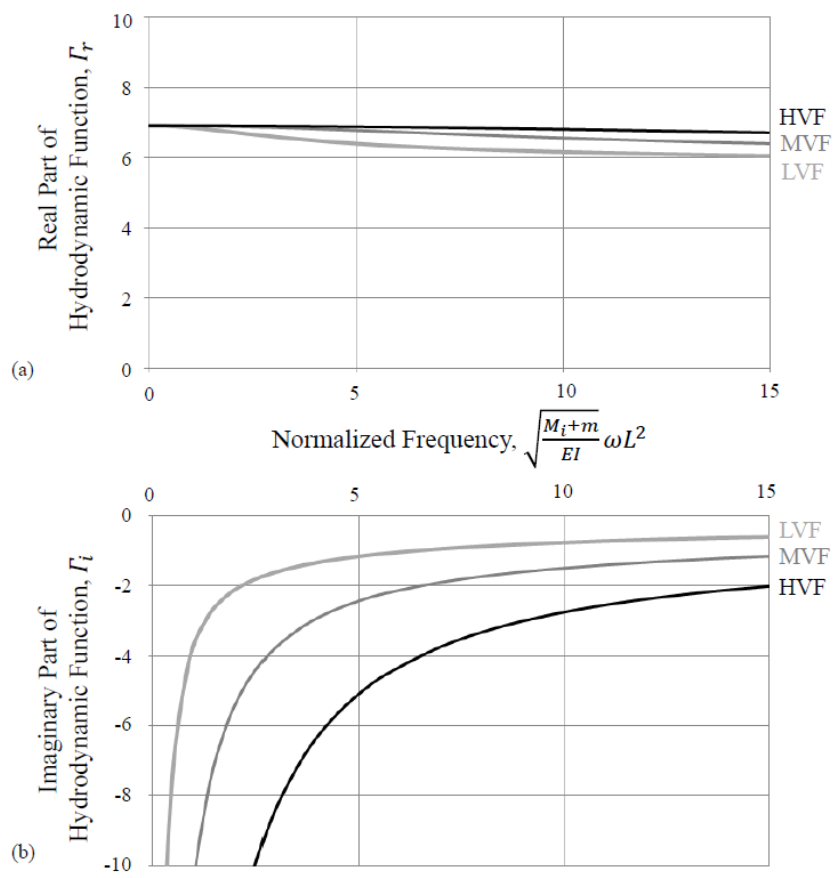

Figure 11. The Hydrodynamic Function for Arbitrary Frequencies. (a) Real Part. (b) Imaginary Part.

3.2 Damping for Non-Zero Fluid Flow

For non-zero fluid flow, the two-dimensional plots of Figure 8 and Figure 9 are expanded to include the conveyed fluid velocity as an additional variable. This results in new three-dimensional surfaces where the natural frequency and damping ratio are functions of both the stiffness of the rotational boundary springs and the conveyed fluid velocity. Figure 12 and Figure 13 plot two manifestations of these new surfaces for the HVF system. In Figure 12, the natural frequency is seen to decrease as the conveyed fluid velocity is increased. This behavior is explained by an induced compression stemming from the centrifugal force. Specifically noting the second and third terms in Eq. (1), the conveyed fluid velocity squared is seen to be proportional to the applied axial force ($\overline{T} \sim M_i U^2$): as the fluid velocity increases, the induced compression increases resulting in a decreasing natural frequency. This decreasing natural frequency results in an increasing damping ratio due to the frequency-dependent nature of the hydrodynamic function (see Figure 10). This relationship is apparent in Figure 13 which shows the damping ratio increasing with increasing fluid velocity. The damping ratio in Figure 13 is shown up to the systems bifurcation velocity after which the system no longer behaves in an underdamped manner (i.e. $\zeta > 1$ past the bifurcation velocity).

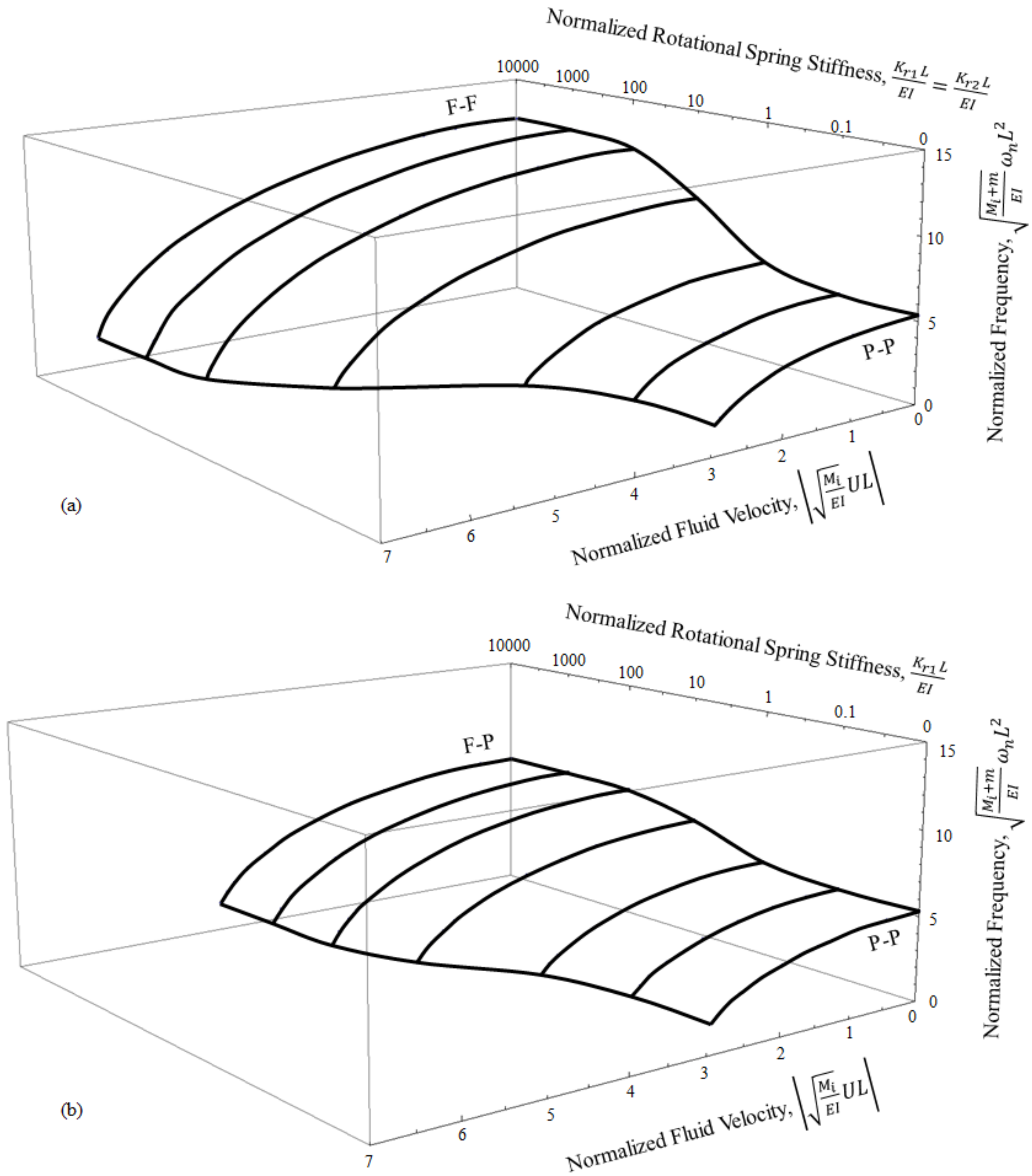

Figure 12. Fluid Velocity (U) vs. Rotational Spring Stiffness (K_r) vs. Natural Frequency (ω_n) – High Viscosity Fluid. (a) $K_{r1} = K_{r2} = K_r$; (b) $K_{r1} = K_r$ & $K_{r2} = 0$ (Pinned).

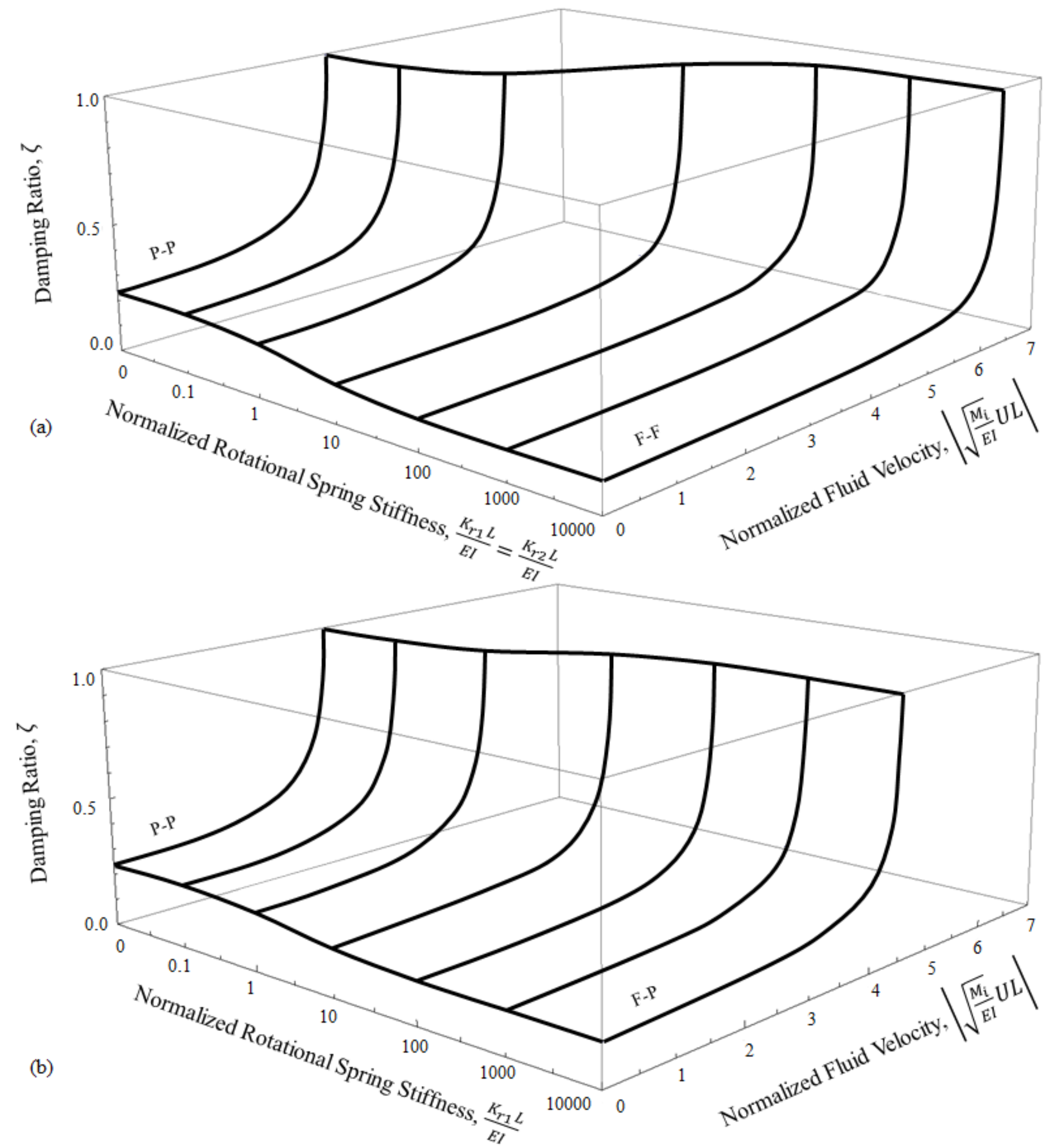

Figure 13. Fluid Velocity (U) vs. Rotational Spring Stiffness (K_r) vs. Damping Ratio (ζ) – High Viscosity Fluid. (a) $K_{r1} = K_{r2} = K_r$; (b) $K_{r1} = K_r$ & $K_{r2} = 0$ (Pinned).

Since both the natural frequency and damping ratio are a function of the rotational stiffness of the boundary springs, Figure 12 and Figure 13 can be combined to directly relate the natural frequency, damping ratio, and conveyed fluid velocity. The resulting three-dimensional surfaces are shown in Figure 14 (note that some of the contours are nearly indistinguishable from each other). If the Figure 14 surfaces are collapsed onto the plane containing the natural frequency and damping ratio, the resulting two-dimensional projection is the same as that found in Figure 10.

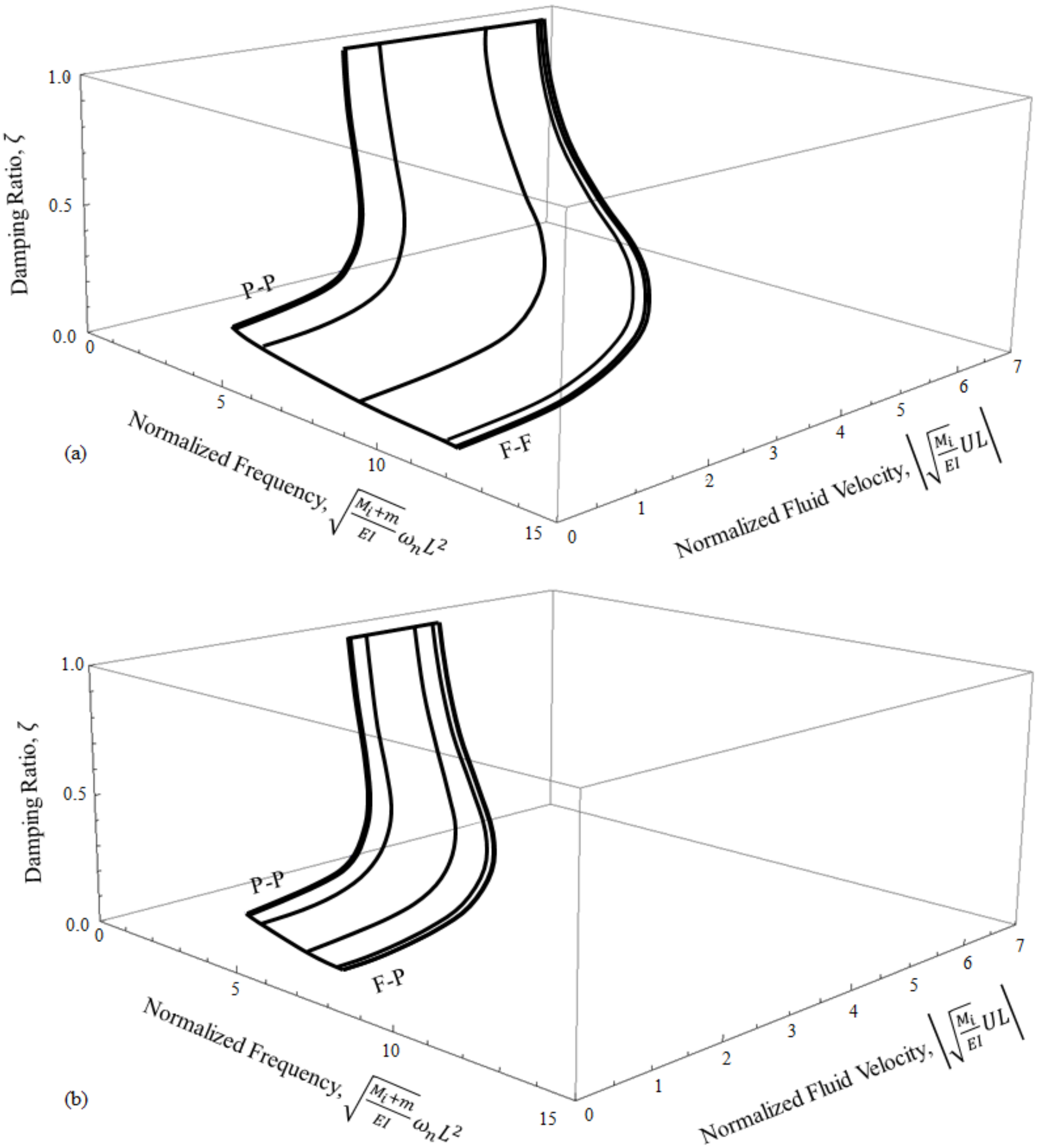

Figure 14. Fluid Velocity (U) vs. Natural Frequency (ω_n) vs. Damping Ratio (ζ) – High Viscosity Fluid. (a) $K_{r1} = K_{r2} = K_r$; (b) $K_{r1} = K_r$ & $K_{r2} = 0$ (Pinned).

Figure 15 shows the limiting cases of Figure 14 projected onto the plane containing the fluid velocity and damping ratio (the MVF and LVF results are also displayed). Several trends are noted:

- For the same boundary conditions and conveyed fluid velocity, higher viscosity systems have higher damping ratios.
- For the same annulus fluid viscosity and conveyed fluid velocity, systems with stiffer rotational boundary springs have lower damping ratios.

- For the same annulus fluid viscosity, the bifurcation velocity increases as the rotational boundary springs are stiffened.
- For the same boundary conditions, the bifurcation velocity decreases with increasing annulus fluid viscosity.
- As the fluid velocity increases, the rate at which the damping ratio changes increases.

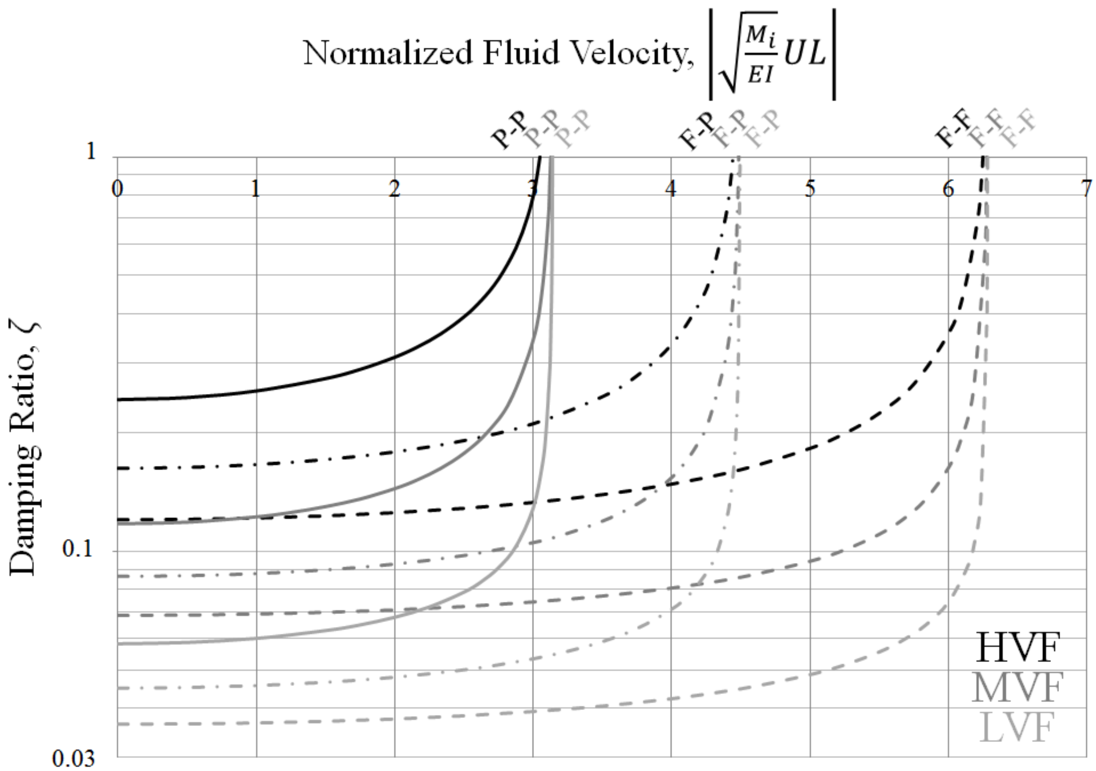

Figure 15. The Effect of Fluid Velocity on Damping for Three Limiting Cases.

This last trend is further illustrated in Figure 16 where the percentage change in the damping ratios for the limiting cases are plotted; the damping ratios at $U = 0$ are taken as baseline values. Two additional trends are noted:

- For the same boundary conditions and conveyed fluid velocity, high-viscosity systems see a greater percentage change in damping ratio compared to their low viscosity counterparts.
- For the same annulus fluid viscosity and conveyed fluid velocity, systems with stiffer rotational boundary springs see a lower percentage change in damping ratio compared to systems with softer rotational springs.

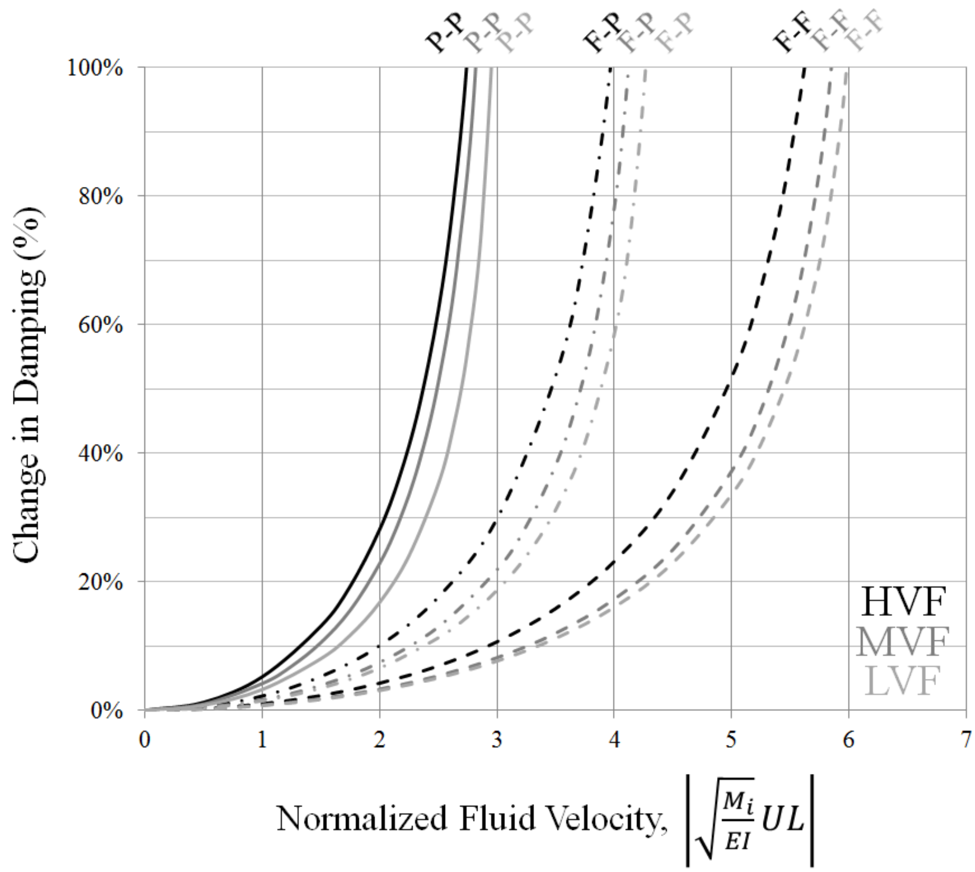

Figure 16. Change in Damping Ratio with Baseline at $U = 0$.

3.3 An Illustrative Example for Designers

These results are especially relevant when there is uncertainty in the characterization of a system. Should the produced fluid velocity be greater than originally estimated or if the rotational stiffness of the boundary springs are initially over-predicted, Figure 15 has shown that the actual damping ratio will be higher than originally predicted. Additionally, Figure 16 has shown that such an error in estimating the damping ratio is exacerbated as the error in either the viscosity or fluid velocity increases.

As a numeric example assume a preliminary investigation of a system indicates a moderate viscosity annulus fluid (MVF), a normalized fluid velocity of one, rotational boundary springs with normalized stiffness of nine, and other inputs as listed in Appendix B. The damping ratio for this system (case A) is calculated as 0.082 and is shown on the three-dimensional domain of Figure 17.

If the system is actually operated at a normalized fluid velocity of two (case B; $\zeta = 0.086$) or has a normalized rotational stiffness of one (case C; $\zeta = 0.108$), the resulting error in estimating the damping ratio would be 4% and 31%, respectively. If the initial estimate of both the fluid velocity and spring stiffness's were in error (case D; $\zeta = 0.119$), the error jumps to 45%. The three-dimensional surface of Figure 17 is compressed into a two-dimensional plot in Figure 18 to more clearly illustrate the difference in the resulting damping ratios.

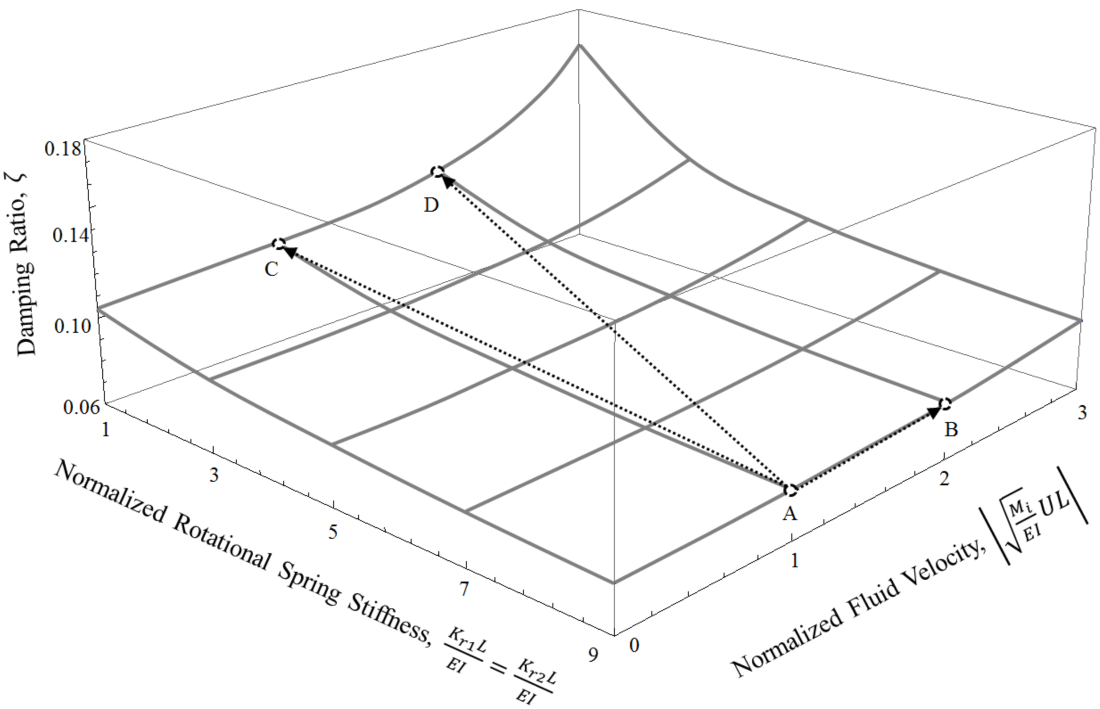

Figure 17. Damping Estimates: Potential Errors Stemming from Conveyed Fluid Velocity and/or Spring Stiffness's (3D).

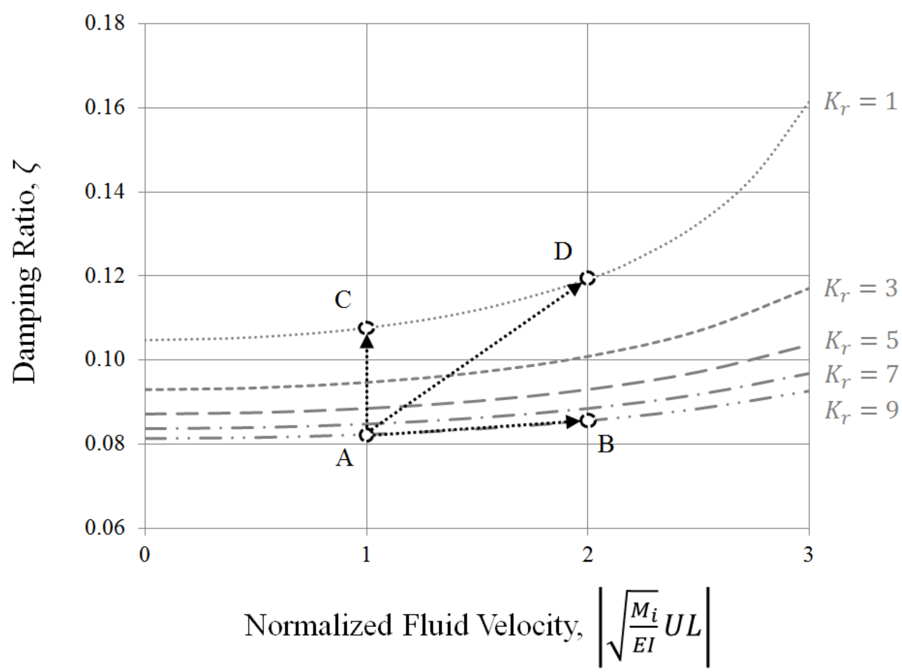

Figure 18. Damping Estimates: Potential Errors Stemming from Conveyed Fluid Velocity and/or Spring Stiffness's (2D).

If the annulus fluid viscosity is initially underestimated (i.e. assumed = MVF, actual = MVF+), additional errors ensue. Figure 19 and Figure 20 depict the damping ratios in the new system (A'-D') for an error in the annulus fluid viscosity (case A'; $\zeta = 0.099$); annulus fluid viscosity and conveyed fluid velocity (case B'; $\zeta = 0.104$); annulus fluid viscosity and rotational spring stiffness's (case C'; $\zeta = 0.134$); and annulus fluid viscosity, conveyed fluid velocity, and rotational spring stiffness's (case D'; $\zeta = 0.150$). The resulting errors (when compared to the baseline case A) are tabulated in Table 1 and in most cases are shown to be non-trivial.

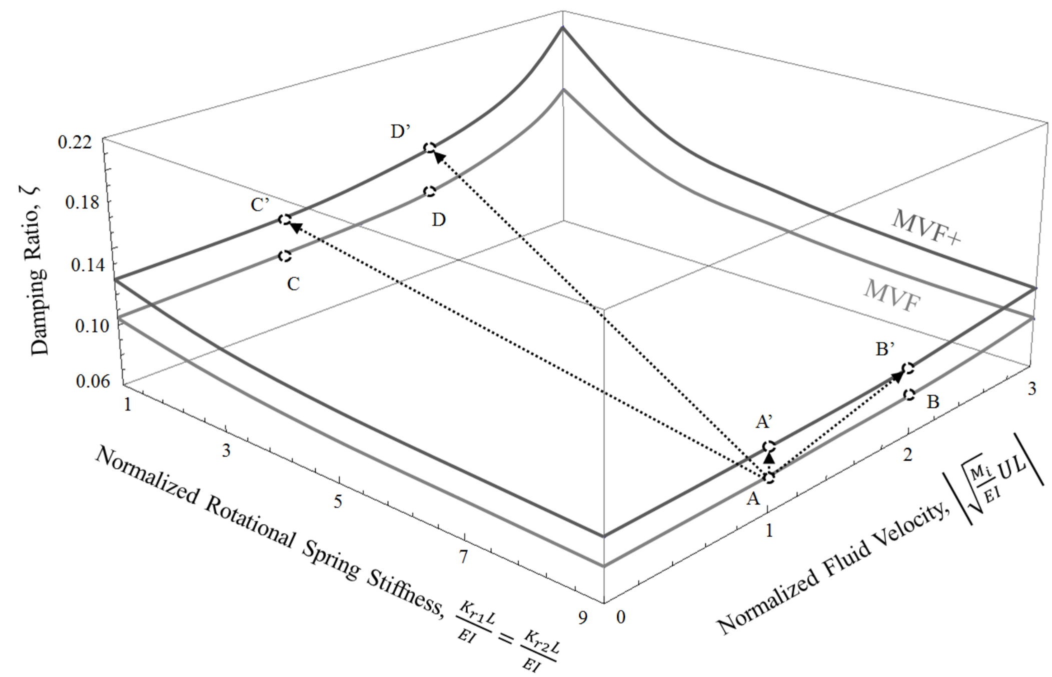

Figure 19. Potential Errors in Damping Estimates Stemming from Annulus Fluid Viscosity, Conveyed Fluid Velocity, and Spring Stiffness's (3D).

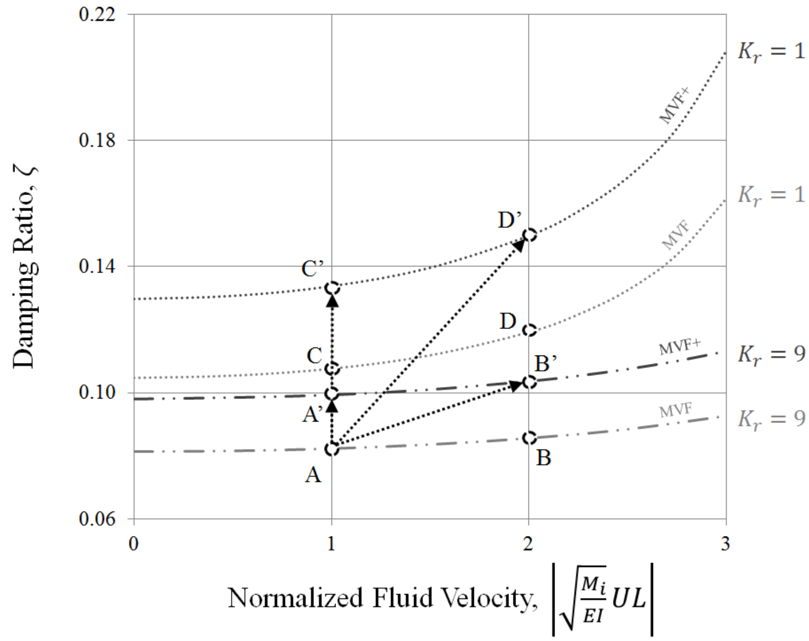

Figure 20. Potential Errors in Damping Estimates Stemming from Annulus Fluid Viscosity, Conveyed Fluid Velocity, and Spring Stiffness's (2D).

Table 1. Numeric Example: Damping Ratios and Corresponding Errors.

Configuration	Damping Ratio	Error (%)
A	0.082	-
B	0.086	4%
C	0.108	31%
D	0.119	45%
A'	0.099	21%
B'	0.104	26%
C'	0.134	63%
D'	0.150	82%

4.0 Conclusions

To develop an optimal vibration based energy harvester for downhole deployment in a hydrocarbon well, it is important to accurately quantify the damping in the system since damping levels ultimately govern the magnitude of the resonant coupled structure-harvester response. To this end a study was undertaken to investigate how fluid velocity affects damping in a fluid-conveying pipe surrounded by a viscous annulus fluid. It was found that, due to the nature of the hydrodynamic function representing the annulus fluid, increasing the conveyed fluid velocity increases the systems damping ratio. It was also noted that stiffer systems saw the damping ratio increase at a slower rate when compared to flexible systems as the conveyed fluid velocity was increased. The results indicate that overestimating the stiffness of a system can lead to underestimated damping ratios and that this error is made worse if the produced fluid velocity or annulus fluid viscosity is underestimated. A numeric example was provided to graphically illustrate these errors.

5.0 Acknowledgements

Funding was provided by Los Alamos National Laboratory through the Engineering Institute under Task 5 (Subcontract No. 77137-001-11). The funding source was not involved with study design; collection, analysis or interpretation of data; in the writing of the report; or in the decision to submit the article for publication.

Appendix A

The hydrodynamic function can be written as [32]

$$\Gamma = \frac{\Gamma_{num}}{\Gamma_{den}} - 1 = \Gamma_r - \mathrm{i}\Gamma_i, \tag{A.1}$$

where

$$\begin{aligned}
\Gamma_{num} &= 2\alpha^2[I_0(\alpha)K_0(\beta) - I_0(\beta)K_0(\alpha)] - 4\alpha[I_1(\alpha)K_0(\beta) + I_0(\beta)K_1(\alpha)] \\
&\quad + 4\alpha\gamma[I_0(\alpha)K_1(\beta) + I_1(\beta)K_0(\alpha)] - 8\gamma[I_1(\alpha)K_1(\beta) - I_1(\beta)K_1(\alpha)], \\
\Gamma_{den} &= \alpha^2(1-\gamma^2)[I_0(\alpha)K_0(\beta) - I_0(\beta)K_0(\alpha)] \\
&\quad + 2\alpha\gamma[I_0(\alpha)K_1(\beta) - I_1(\beta)K_0(\beta) + I_1(\beta)K_0(\alpha) - I_0(\beta)K_1(\beta)] \\
&\quad + 2\alpha\gamma^2[I_0(\beta)K_1(\alpha) - I_0(\alpha)K_1(\alpha) + I_1(\alpha)K_0(\beta) - I_1(\alpha)K_0(\alpha)].
\end{aligned} \tag{A.2}$$

The relevant arguments are

$$\bar{k} = \sqrt{\frac{\mathrm{i}\omega}{\upsilon_e}}; \quad \alpha = \bar{k}d; \quad \beta = \bar{k}D; \quad \gamma = \frac{d}{D}. \tag{A.3}$$

The assumptions used in the derivation of the hydrodynamic forcing include:

- The vibrating pipe is enclosed by a rigid concentric cylindrical boundary. The annulus between the pipe and boundary contains a viscous fluid.
- The annulus fluid has zero velocity at the rigid concentric boundary. At the pipes outer surface, the annulus fluid velocity matches the pipe velocity.
- The annulus fluid is quiescent, homogeneous, Newtonian, and incompressible.
- The pipe length is much greater than the pipe diameter.
- The pipe is an isotropic linearly elastic solid and is of uniform cylindrical cross section.
- The amplitude of vibration is much smaller than any length scale in the pipe geometry permitting the Navier-Stokes and fluid continuity equations to be linearized.

Appendix B

The variables used in the four cases investigated are listed in Table B.1.

Table B.1. Inputs.

		Case			
Variable	**Units**	**LVF**	**MVF**	**MVF+**	**HVF**
c	kg/s	0			
d	m	0.05			
g	$\mathrm{m/s^2}$	9.81			
m	kg/m	15.95			
$\bar{p}$	$\mathrm{N/m^2}$	0			
A_i	$\mathrm{m^2}$	$5.81E-03$			
D	m	0.06			
E	$\mathrm{N/m^2}$	$2E+11$			
I	$\mathrm{m^4}$	$2.22E-06$			
K_r	Nm/rad	Varies			
K_t	N/m	$1.00E+9$ (Rigid)			
L	m	8			
M_i	kg/m	4.94			
$\bar{T}$	N	0			
U	m/s	Varies			
ρ_e	$\mathrm{kg/m^3}$	900			
υ_e	$\mathrm{m^2/s}$	$1E-05$	$3E-05$	$4E-05$	$7E-05$
ν	-	0			

LVF - Low Viscosity Fluid
MVF - Moderate Viscosity Fluid
MVF+ - Moderate Viscosity Fluid
HVF - High Viscosity Fluid

References

[1] G. Park, T. Rosing, M.D. Todd, C.R. Farrar, W. Hodgkiss, Energy harvesting for structural health monitoring sensor networks, *Journal of Infrastructure Systems* 14 (1) (2008) 64-79.

[2] A. Dewan, S.U. Ay, M.N. Karim, H. Beyenal, Alternative power sources for remote sensors: a review, *Journal of Power Sources* 245 (2014) 129-143.

[3] S. Chalasani, J.M. Conrad, A survey of energy harvesting sources for embedded systems, *Southeastcon, 2008. IEEE*, IEEE, 2008.

[4] N.S. Hudak, G.G. Amatucci, Small-scale energy harvesting through thermoelectric, vibration, and radiofrequency power conversion, *Journal of Applied Physics* 103 (10) (2008) 101301.

[5] A. Erturk, D.J. Inman, *Piezoelectric energy harvesting*, John Wiley & Sons, West Sussex, United Kingdom, 2011.

[6] H.A. Sodano, D.J. Inman, G.Park, A review of power harvesting from vibration using piezoelectric materials, *Shock and Vibration Digest* 36 (3) (2004) 197-206.

[7] S. Priya, Advances in energy harvesting using low profile piezoelectric transducers, *Journal of electroceramics* 19 (1) (2007) 167-184.

[8] S.R. Anton, H.A. Sodano, A review of power harvesting using piezoelectric materials (2003–2006), *Smart Materials and Structures*, 16 (3) (2007) R1.

[9] D.P. Arnold, Review of microscale magnetic power generation, *IEEE Transactions on Magnetics* 43 (11) (2007) 3940–3951.

[10] S.P. Beeby, M.J. Tudor, R.N. Torah, S. Roberts, T. O'Donnell, S. Roy, Experimental comparison of macro and micro scale electromagnetic vibration powered generators, *Microsystem Technologies* 13 (11-12) (2007) 1647-1653.

[11] D. Spreemann, Y. Manoli. *Electromagnetic vibration energy harvesting devices: Architectures, design, modeling and optimization*, Vol. 35, Springer Science & Business Media, 2012.

[12] R.J. Wetzel, S. Hiron, A.F., Veneruso, D.R. Patel, T.D. MacDougall, J. Walter, Harvesting vibration for downhole power generation, U.S. Patent Application No. 12/400,024 (2009).

[13] S. Priya, D.J. Inman, *Energy Harvesting Technologies*, Vol. 21, Springer, New York, 2009.

[14] E.J. Kjolsing, M.D. Todd, Frequency response of a fixed-fixed pipe immersed in viscous fluids, conveying internal steady flow, *Journal of Petroleum Science and Engineering* (134) (2015) 247-256.

[15] M. Hosseini, M. Sadeghi-Goughari, S.A. Atashipour, M. Eftekhari, Vibration analysis of single-walled carbon nanotubes conveying nanoflow embedded in a viscoelastic medium using modified nonlocal beam model, *Archives of Mechanics* 66 (4) (2014) 217-244.

[16] I. Lottati, A. Kornecki, The effect of an elastic foundation and of dissipative forces on the stability of fluid-conveying pipes, *Journal of Sound and Vibration* 109 (2) (1986) 327-338

[17] M.P. Païdoussis, A.K. Misra, S.P. Chan, Dynamics and stability of coaxial cylindrical shells conveying viscous fluid, *Journal of Applied Mechanics* 52 (2) (1985) 389-396.

[18] M.P. Païdoussis, A.K. Misra, V.B. Nguyen, Internal-and annular-flow-induced instabilities of a clamped-clamped or cantilevered cylindrical shell in a coaxial conduit: The effects of system parameters, *Journal of Sound and Vibration* 159 (2) (1992) 193-205.

[19] P. Soltani, M.M. Taherian, A. Farshidianfar, Vibration and instability of a viscous-fluid-conveying single-walled carbon nanotube embedded in a visco-elastic medium, *Journal of Physics D: Applied Physics* 43 (42) (2010) 425401.

[20] T.T. Yeh, S.S. Chen, The effect of fluid viscosity on coupled tube/fluid vibrations, *Journal of Sound and Vibration* 59 (3) (1978) 453-467.

[21] R. Bahaadini, M. Hosseini, Effects of nonlocal elasticity and slip condition on vibration and stability analysis of viscoelastic cantilever carbon nanotubes conveying fluid, *Computational Materials Science* (114) (2016) 151-159.

[22] M. Hosseini, M. Sadeghi-Goughari. Vibration and instability analysis of nanotubes conveying fluid subjected to a longitudinal magnetic field, *Applied Mathematical Modelling* 40 (4) (2016) 2560-2576.

[23] M. Eftekhari, M. Hosseini, On the stability of spinning functionally graded cantilevered pipes subjected to fluid-thermomechanical loading, *International Journal of Structural Stability and Dynamcis* (2015) 1550062.

[24] M. Kheiri, M.P. Païdoussis, G. Costa Del Pozo, M. Amabili, Dynamics of a pipe conveying fluid flexibly restrained at the ends, *Journal of Fluids and Structures* 49 (2014) 360-385.

[25] R. Bao, Analysis of fluid-solid coupling characteristics of oil and gas submarine span pipelines, *Journal of Pipeline Systems Engineering and Practice* (2014) A4014001.

[26] U. Lee, *Spectral element method in structural dynamics*, John Wiley & Sons, Singapore, 2009.

[27] U. Lee, I. Jang, H. Go, Stability and dynamic analysis of oil pipelines by using spectral element method, *Journal of Loss Prevention in the Process Industries* 22 (6) (2009) 873-878.

[28] G.G. Stokes, *On the effect of the internal friction of fluids on the motion of pendulums*, Vol. 9., Pitt Press, 1851.

[29] S.S. Chen, Fluid damping for circular cylindrical structures, *Nuclear Engineering and Design* 63 (1) (1981) 81-100.

[30] L. Rosenhead, *Laminar Boundary Layers*, Clarendon Press, Oxford, 1963.

[31] E.O. Tuck, Calculation of unsteady flows due to small motions of cylinders in a viscous fluid, *Journal of Engineering Mathematics* 3 (1) (1969) 29-44.

[32] M.W. Wambsganss, S.S. Chen, J.A. Jendrzejczyk, Added mass and damping of a vibrating rod in confined viscous fluids, *NASA STI/Recon Technical Report N* 75 (1974) 10349.

[33] R. Chilukuri, Added mass and damping for cylinder vibrations within a confined fluid using deforming finite elements, *Journal of Fluids Engineering* 109 (3) (1987) 283-288.

[34] G.A. Cranch, J.E. Lane, G.A. Miller, J.W. Lou, Low frequency driven oscillations of cantilevers in viscous fluids at very low Reynolds number, *Journal of Applied Physics* 113 (19) (2013) 194904.

[35] G.A. Cranch, G.A. Miller, C.K. Kirkendall, Fiber-optic, cantilever-type acoustic motion velocity hydrophone, *The Journal of the Acoustical Society of America* 132 (1) (2012) 103-114.

[36] V.F. Siniavskii, V.S. Fedotovskii, A.B. Kukhtin, Oscillation of a cylinder in a viscous liquid, *Prikladnaia Mekhanika* 16 (1980) 62-67.

[37] B. Weiss, E.K. Reichel, B. Jakoby, Modeling of a clamped–clamped beam vibrating in a fluid for viscosity and density sensing regarding compressibility, *Sensors and Actuators A: Physical* 143 (2) (2008) 293-301.

[38] S. Basak, A. Raman, S.V. Garimella, Hydrodynamic loading of microcantilevers vibrating in viscous fluids, *Journal of Applied Physics* 99 (11) (2006) 114906.

[39] J.W.M. Chon, P. Mulvaney, J.E. Sader, Experimental validation of theoretical models for the frequency response of atomic force microscope cantilever beams immersed in fluids, *Journal of Applied Physics* 87 (8) (2000) 3978-3988.

[40] C.P. Green, J.E. Sader, Frequency response of cantilever beams immersed in viscous fluids near a solid surface with applications to the atomic force microscope, *Journal of Applied Physics* 98 (11) (2005) 114913.

[41] A. Maali, C. Hurth, R. Boisgard, C. Jai, T. Cohen-Bouhacina, J.P. Aime, Hydrodynamics of oscillating atomic force microscopy cantilevers in viscous fluids, *Journal of Applied Physics* 97 (7) (2005) 074907.

[42] J.E. Sader, Frequency response of cantilever beams immersed in viscous fluids with applications to the atomic force microscope, *Journal of Applied Physics* 84 (1) (1998) 64-76.

[43] M.P. Païdoussis, N.T. Issid, Dynamic stability of pipes conveying fluid, *Journal of Sound and Vibration* 33 (3) (1974) 267-294.

[44] C.Q. Guo, C.H. Zhang, M.P. Païdoussis, Modification of equation of motion of fluid-conveying pipe for laminar and turbulent flow profiles, *Journal of Fluids and Structures* 26 (5) (2010) 793-803.

[45] U. Lee, H. Oh, The spectral element model for pipelines conveying internal steady flow, *Engineering Structures* 25 (8) (2003) 1045-1055.

[46] G.L. Kuiper, A.V. Metrikine, Experimental investigation of dynamic stability of a cantilever pipe aspirating fluid, *Journal of Fluids and Structures* 24 (4) (2008) 541-558.

[47] M.P. Païdoussis, C. Semler, M. Wadham-Gagnon, A reappraisal of why aspirating pipes do not flutter at infinitesimal flow, *Journal of Fluids and Structures* 20 (1) 147-156.

[48] M.P. Païdoussis, G.X. Li, Pipes conveying fluid: a model dynamical problem, *Journal of Fluids and Structures* 7 (2) (1993) 137-204.

[49] M.P. Païdoussis, *Fluid-structure interactions: slender structures and axial flow*, Vol. 1, Academic press, San Diego, California, 2014.